www.rericjournal.ait.ac.th

Investigation of PV and Wind Hybrid System for Building Rooftop

Wichai Pettongkam[*,1], Wirachi Roynarin[*], and Decha Intholo[*]

Abstract – *Solar and wind are clean energy sources with significant potential to alleviate grid dependence. This study aims to investigate the use of wind energy resources with the support of solar energy through hybrid technology for a high-rise building in Pathumthani Province, Thailand. Further, a computational fluid dynamics (CFD) simulation to determine the optimum location for wind turbine installation is conducted. The study used a hybrid model on the HOMER software to simulate the outputs of electricity, and the latter were evaluated with on-site experimental data. The CFD simulation indicates the result of some wind turbine installation points on rooftop where the surrounding small buildings and terrain can increase both the magnitude and velocity vector direction. The results of the HOMER simulation of the power production indicate that approximately 47% of the power was generated from the Photo Voltaic(PV) solar system, approximately 8% from the wind turbine system, and 45% supplied by the local grid. The renewable fraction of this system is therefore approximately 0.524. The experimental data indicate that 42.38% of the annual power production is from the PV system, and 5.87% is from the wind turbine system, indicating the potential to reduce the annual dependence on grid electricity by 51.75%.*

Keywords – *Computational Fluid Dynamic (CFD), hybrid system, HOMER software, micro wind turbine, pv solar panel.*

1. INTRODUCTION

Renewable energy resources, such as solar and wind, are distributed worldwide [1], including in remote locations where hybrid energy systems comprising combined solar and wind energy conversion units with battery storage are utilized [2]. The operation of solar and wind energy systems has become increasingly popular owing to their modular and environmentally friendly nature [3].

The real estate business in Thailand, especially that concerning residential buildings in the Bangkok metropolitan area, has transformed building projects across the country significantly since 2000. Developers have shifted housing design projects from 2–3 bedroom bungalows to high-rise apartments. In 2015, over 52,000 housing units were completed in Bangkok alone, and most of the erected structures were condominiums. For high-rise buildings located in urban areas, roof-mounted micro wind turbines can be a suitable energy source because they produce less noise than large wind turbines, [4] and exhibit low cut-in and rated speed; these can be effective for generating power from winds of medium or high speed, even with short durations [5], [6].

The electrical energy used in high-rise buildings can be considered in two parts: electrical energy used in private areas, and electrical energy used in typically public areas.

This research was conducted in the high-rise PIER 93 Building, located in the Klong 4 district of Thanyaburi, Pathum Thani Province, which is shown in Figure 1. This district is located on the east side of Bangkok and is classified as a central district.

1.1 Solar Energy Resources

Solar energy is the most typical and abundant energy resource in the world. Solar radiation is the primary source of electromagnetic energy in our environment, and solar photovoltaic (PV) technology is used to convert sunlight into direct current electricity. It is the most popular renewable energy system at the building and neighbourhood scale. The total energy consumption of the earth is approximately 15 terawatts, implying that human beings could sustain our society using 0.01% of the solar energy in nature without burning fossil fuels. The goal of solar PV technology is to achieve higher performance with lower costs.

The process of electricity generation in a PV system is illustrated in Figure 2. PV cells generate direct current electricity by utilising particular characteristics of semi-conducting materials; when the PV cell is exposed to sunlight, photons of the sunlight come into contact with the solar absorbent semi-conducting material, thus exciting its electrons, and subsequently generate current through an external load.

1.2 Solar Energy Potential of Thailand

The global solar radiation incident over the area of Thailand is shown in Figure 3. As illustrated, the highest solar radiation, 19–20 MJ/m2·day, was measured in the middle of Thailand. The annual average global radiation of Thailand from 1964–2008 was 6.82 MJ/m2 (4.672 kWh/m2·d)[7], as shown in Figure 4. The selected study area is located at 14 ˚N, 100 ˚E. In this area the highest average solar energy is received in April of each year, at 5.458 kWh/day, and the lowest in September, at 4.161 kWh/day [8].

*Engineering Faculty, Rajamangala University of Technology Thanyaburi, Phathumthani, Thailand 12110.

[1] Corresponding author;
Tel: + 66 089 771 4294.
E-mail: wirachai_r@rmutt.ac.th.

1.3 Wind Energy Resources

Various data sources indicate that the study location possess low wind energy potential. However, because micro wind turbines exhibit low cut-in and low rated speeds, they can be effective in generating small amounts of usable power from winds of lower speeds, or higher speeds and shorter durations. Wind energy is not as easy to capture as solar energy because it keeps flowing, moving, and changing direction; moreover, the complex physical conditions of cities render it even more difficult to predict. Two types of wind turbines (WT) exist: vertical axis wind turbines (VAWT) and horizontal axis wind turbines (HAWT), as shown in Figure 5.

(a) (b)

Fig. 1. (a) Pathumthani province, Thailand; (b) high-rise PIER 93 building, located in Pathumthani province.

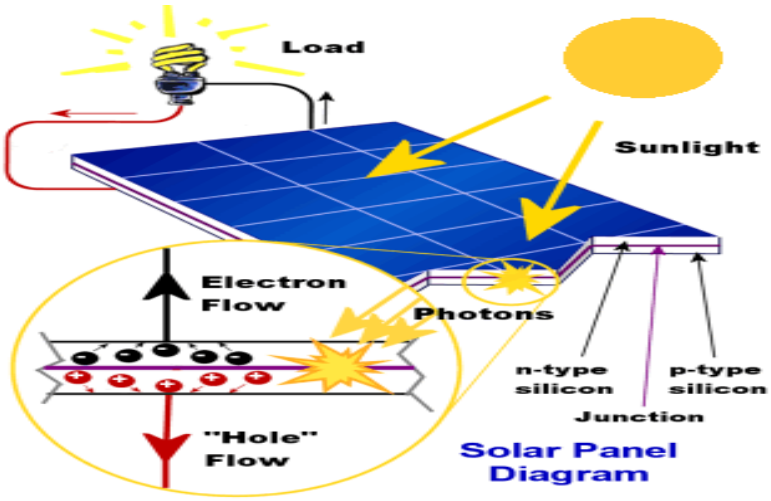

Fig. 2. The electricity generation process from PV.

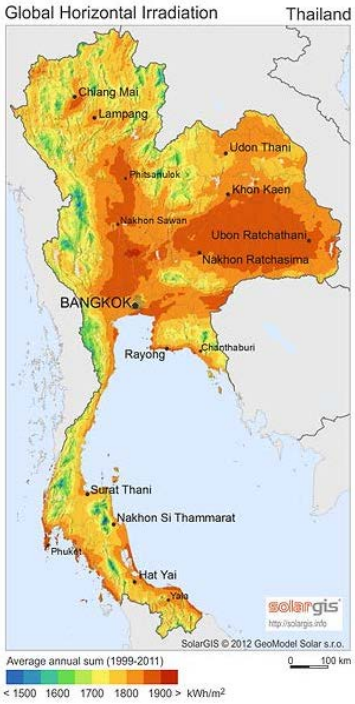

Fig. 3. Average annual solar radiation map of Thailand.

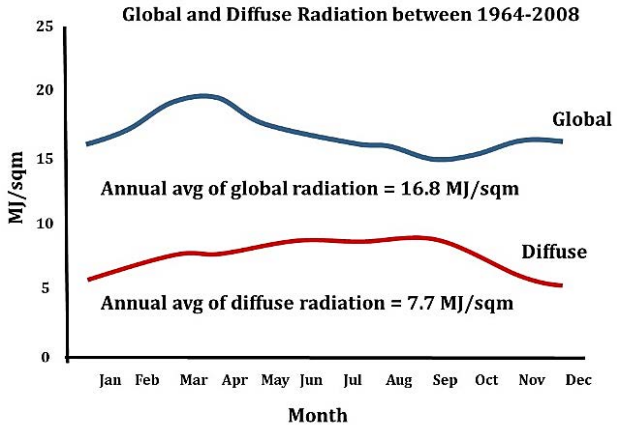

Fig. 4. Monthly average global and diffuse solar radiation from 1964–2008, Thailand.

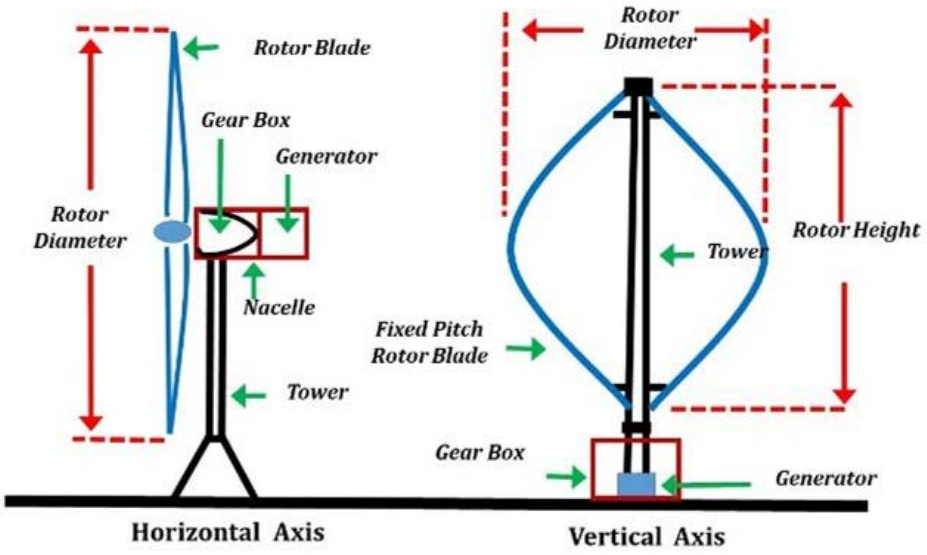

Fig. 5. Horizontal axis and vertical axis wind turbines.

To justify the utilisation of wind turbines in cities, potential problems such as noise and urban design requirements need to be mitigated, and their performance needs to be maximised. One approach to maximising the performance is to develop wind turbines with lower cut-in speed to accommodate the slow average wind speeds in urban areas[9]. However, the extra cost of wind turbines with low cut-in speed may not be offset by the consequent energy gain, potentially rendering them economically inefficient. The wind potential in Thailand, as classified by the World Bank, is considered as primarily poor to fair, as shown in Figure 6.

The wind resource map of Southeast Asia shown in Figure 6 was created for the World Bank by True Wind Solutions using the Metso Map, a mesoscale atmospheric simulation system.Although the map should present an accurate overall picture of wind True Wind Solutions using the Metso Map, a mesoscale atmospheric simulation system.Although the map should present an accurate overall picture of wind resources in Southeast Asia, resource estimates for any particular location should be confirmed by local measurements.

To utilise wind energy to generate electricity, the annual monsoon pattern of any given location is crucial. The annual monsoon characteristics of Thailand are illustrated in Figure 7. The wind direction and wind speed at a selected location must be measured continuously to obtain the correct data with which the potential of wind energy is to be analysed to generate electricity.

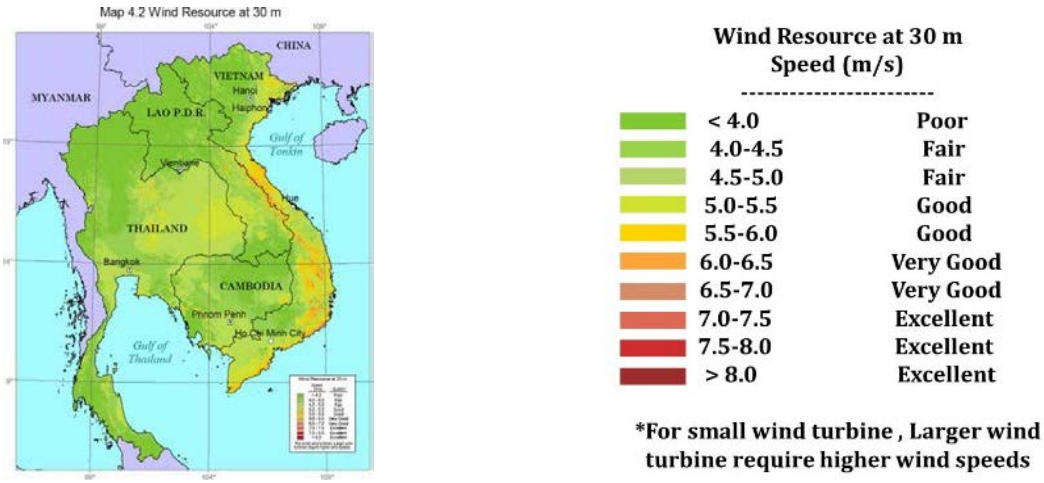

Fig. 6. Wind potential in Thailand.

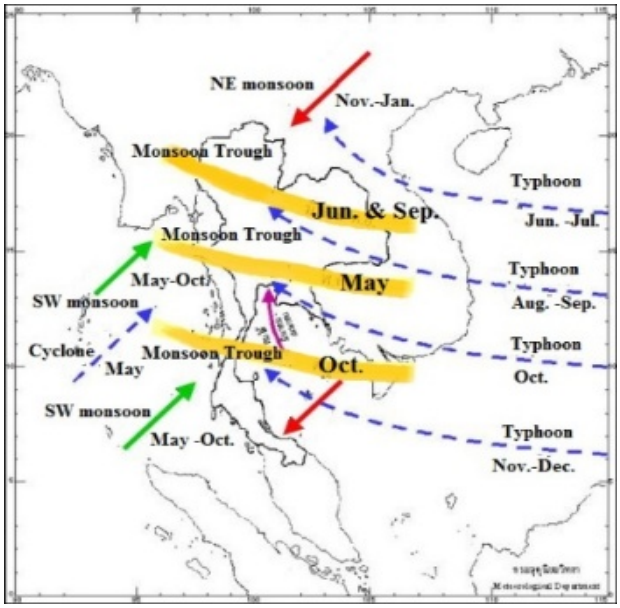

Fig. 7. Annual monsoon characteristics of Thailand.

Table 1. Wind data in Suvanabhumi Airport of Thailand as measured by Windfinder website.

M/Y	Ave (m/s)	M/Y	Ave (m/s)	M/Y	Ave (m/s)
Jan	3.60	May	4.12	Sep	3.60
Feb	3.60	Jun	4.12	Oct	3.09
Mar	4.63	Jul	4.12	Nov	3.09
Apr	4.12	Aug	4.12	Dec	3.60
				Annual Average	3.82

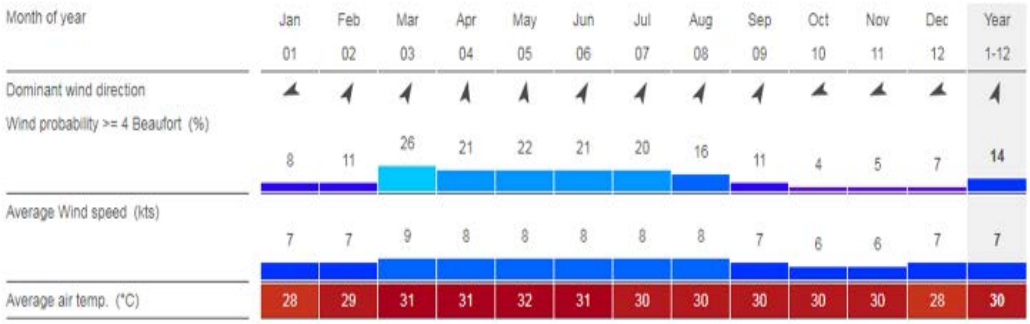

The wind data for the study area were measured and collected by the Windfinder website at the Suvarnabhumi Airport measuring station. The annual wind data for this location is shown in Table 1. The minimum and maximum monthly average wind speeds are 3.09 m/s and 4.63 m/s, respectively. The annual average wind speed of the selected area is 3.82 m/s, which is sufficient to utilise wind energy.

In the cold season from November to January, including the northeast monsoon and tropical cyclone, an average wind speed of 3.43 m/s was measured. From February to April, with the hot summer weather, southwest monsoon, and tropical cyclone, the average wind speed was measured as 4.12 m/s. In the rainy season from May to October, in which the effects of tropical cyclone and the southwest monsoon are experienced, an average wind speed of 3.86 m/s was measured and recorded.

Figure 8 shows the wind data, based on real observations from the weather station; they are collected at Suvarnabhumi Airport in Samut Prakan, Thailand from Windfinder. The PIER93 building located at the Phathumthani Province is near Suvarnabhumi Airport. Therefore, the data from Suvarnabhumi Airport are used for the calculation in this study. Generally, the wind flow direction of Thailand is from the South–Southeast direction (SSW) and East–Northeast direction, as shown in the annual wind rose diagram.

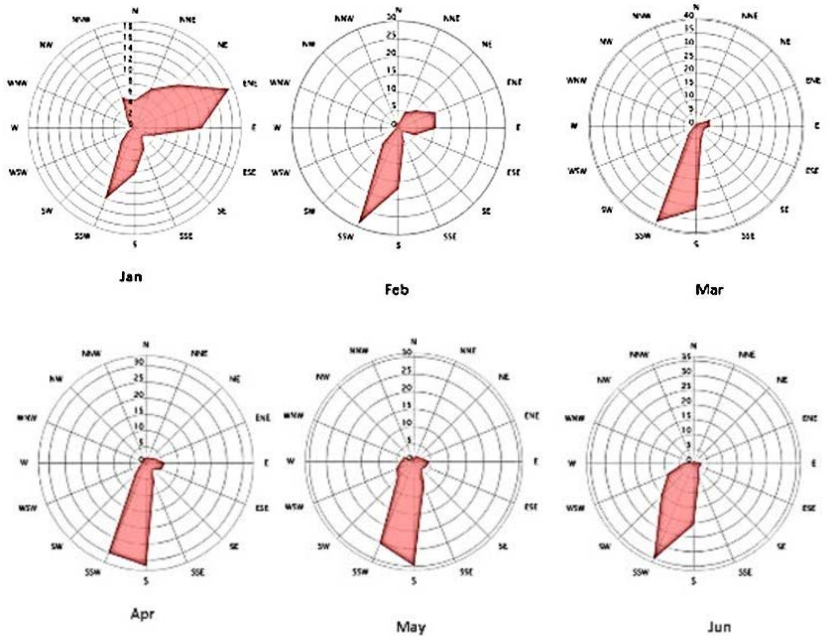

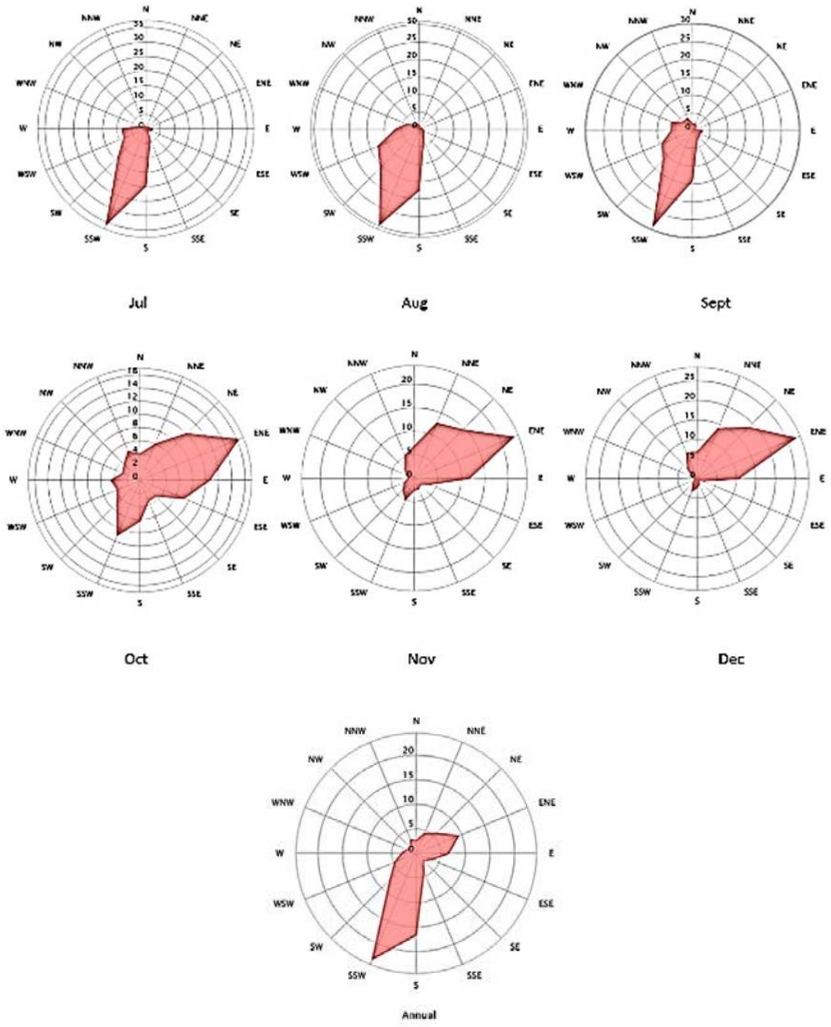

Fig. 8. Wind rose at Suvarnabhumi Airport of Thailand [10].

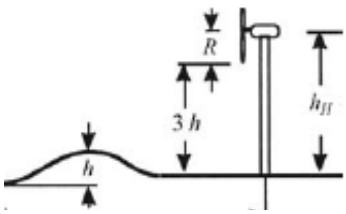

Fig. 9. Determination of flat terrain [11].

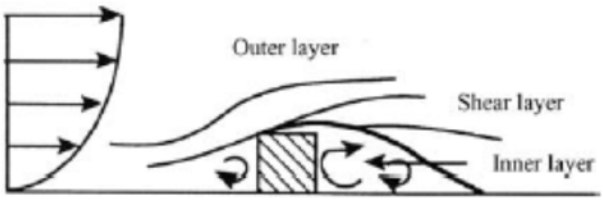

Fig. 10. Schematic of a momentum wake.
(Reproduced with permission from Alternative Energy Institute [11])

1.4 Flow Over Terrain With Obstacles

The terrain is divided primarily into flat and non-flat terrain. The effect of terrain to wind flow must be considered when wind turbines are installed. As Figure 9 shows, the hub-high of the wind turbine should be 3h of the hill height. When wind flows over an obstacle, the recirculating wake flow region (eddy) will be generated at the downstream side of the obstacle, and the velocity of the wind flow will increase at the top of the obstacle, as show in Figure 10.

1.5 Hybrid Energy System

The hybridization of energy sources increases the overall reliability of the system because one energy source can compensate for another as necessary. However, proper component selection and sizing are essential in the design of such systems [12]. Several studies have shown that in addition to improving energy reliability, hybrid renewable energy systems also increase global sustainability. A study of PV distributed generation (PV-DG) hybrid systems was conducted using 12 isolated, off-grid hybrid renewable energy systems installed for rural electrification in the Jujuy province of Argentina [13]. Further, a comparison of stand-alone and grid-connected hybrid systems in Turkey has been conducted [14]. In India, hybrid PV and wind energy systems are becoming popular and are beginning to penetrate the renewable energy market, because hybrid renewable energy systems are cost-effective in remote areas where extending the grid supply would be expensive [15], [16].

1.6 Modeling and Simulation

A system optimization tool based on the hybrid renewable energy system optimization model (HOMER) software has been developed by the United States National Renewable Energy Laboratory [17]. It is a flexible tool that models a combination of conventional fuels and renewable energies to determine the most cost-effective configuration for each system. HOMER performs hundreds or thousands of simulations hourly to ensure the best possible match between the supply and demand to design the optimum system.

Many resources such as WT, PV arrays, fuel cells, small hydropower, biomass converters, batteries, and conventional generators can be modelled in HOMER [18]. The HOMER program also considers hybrid renewable energy systems (HRES) in grid-connected and stand-alone modes. Figure 11 shows a typical configuration of an HRES designed in HOMER, the required input data for simulation with HOMER, and a comprehensive framework demonstrating how HOMER determines the optimal size of the equipment for HRES [19].

1.7 Research Scope

This paper presents an integrated solar PV–wind energy system that was designed using the HOMER software tool under a set load demand, with an area limitation corresponding to the rooftop area of the PIER 93 building. Using the computational fluid dynamics (CFD) method for simulating wind flow at the PIER 93 terrain, the good location from the SSW wind flow direction of the micro wind turbine-installation on the rooftop area was determined. In addition to conducting a simulation analysis of this PV–wind hybrid model, the study also investigates the performance and power output of a PV–wind hybrid system at the installation site.

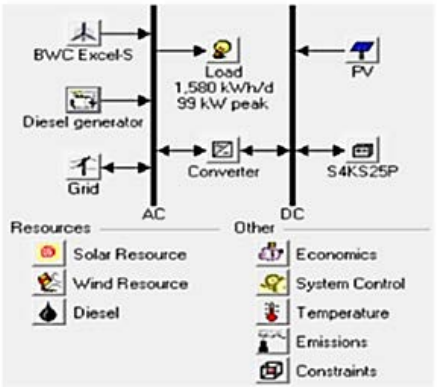

Fig. 11. Typical schematic of an HRES in HOMER [20].

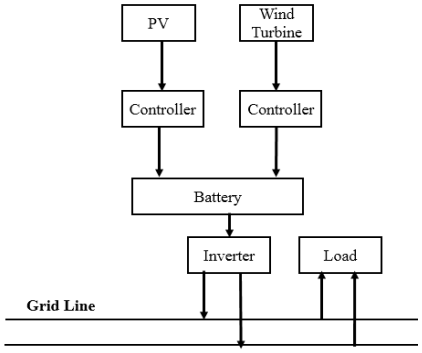

Fig. 12. Conceptual design of a hybrid two-energy renewable energy system.

2. MATERIALS AND METHODS

Figure 9 shows the conceptual design of an energy system that uses two renewable energy sources: wind and solar, to generate electricity that is subsequently converted by a converter. A grid-interactive PV system ensures the effective utilisation of the generated power, as illustrated by a study in Nigeria that used HOMER to analyse the feasibility, reliability, and economic performance of an 80-kW solar PV grid-interactive system.

Figure 12 shows the conceptual design of a hybrid two-energy renewable energy system. The natural source energies of solar and wind used the PV panel to collect solar energy and wind turbine energy, respectively. Each device is provided with its own controller by; subsequently, the battery collects the energy and finally the energy is converted by an inverter to the grid line.

The PIER 93 building has seven floors, and the hybrid PV–wind system is separated into four sets. Set 1 produced the electricity for the first floor, set 2 produced the electricity for the second and third floors, set 3 produced the electricity for the fourth and fifth floors, and set 4 produced the electricity for the sixth and seventh floors, as shown in Figure 13.

To estimate the solar energy, only the potential from the rooftop of the building was used; likewise, for wind, estimations based on wind turbines installed on the rooftop of the building were used. The wind energy potential was calculated with formulas using an estimated wind speed based on the average wind speed at the height of the building, *i.e.* 21 m, which is 3.82 m/s. The grid-connected hybrid renewable energy system of this study consisted of wind turbines and solar PV panels.

Before designing the system, the selected locations, load profiles, and potential of the renewable energy resources were evaluated as summarized below. The electrical load was calculated based on the total electricity consumption.

The PIER 93 building is shown in Figure 14a. The rooftop was initially designed as shown in Figure 14b, but subsequently reconstructed and enlarged to collect up to 57.6 m^3 of rainwater, as shown in Figure 14c.

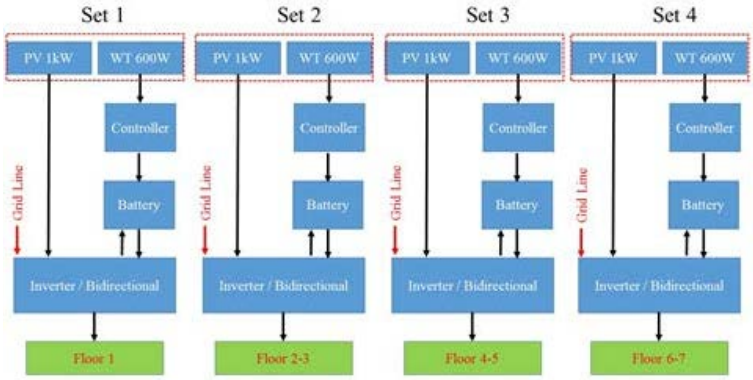

Fig. 13. Schematic of Hybrid Wind-PV system for PIER 93 building usage.

(a) (b) (c)

Fig. 14. PIER 93 high-rise building (a) PIER 93 high-rise building (b) roof gutter area (c) water storage area on rooftop.

Table 2. Typical-area electrical load at PIER 93 high-rise building.

Floor	Table Column Head				
	LED 2x18W	LED 2x9W	LED 7W	LED 1x18W	LED 1x9W
1	44	7	31	-	2
2	5	-	11	1	-
3	5	-	11	1	-
4	5	-	11	1	-
5	5	-	11	1	-
6	5	-	11	1	-
7	5	-	11	1	-
Total	148	14	97	6	2
kWh/d	16.13	3.02	6.55	2.59	0.86
Total	29.15 kWh/d				

Table 2 shows the typical electrical load of the building, including 115 sets of 18-W LED bulbs and 24 sets of 9-W LED bulbs, for an overall load of 29.16 kWh/day. The maximum power output is the peak power at which a solar cell can deliver under the standard test conditions (STCs). Although PV installations are typically rated based on this value, it is unlikely that these power levels will be achieved in practice.

2.1 Terrain of Pier 93 Building

Considering the terrain at the PIER 93 building, the canal in front of the building includes the primary road.

The PIER 93 building is surrounded by many small buildings, as shown in Google views (see Figure 15a). The two-dimensional (2D) model is as shown in Figure 15b, and the three-dimensional (3D) model is as shown in Figure 15c.

After the 3D model was created, the grid cell of the 3D model was created, as shown in Figure 16(a). The grid cell was created at the terrain of building as Figure 16(b), the building, and the wind turbine. Figure 16(c) shows the grid cell generated at the turbine that included the rotating region, wind turbine tail, wind turbine blade, wind turbine nacelle, and wind turbine tower.

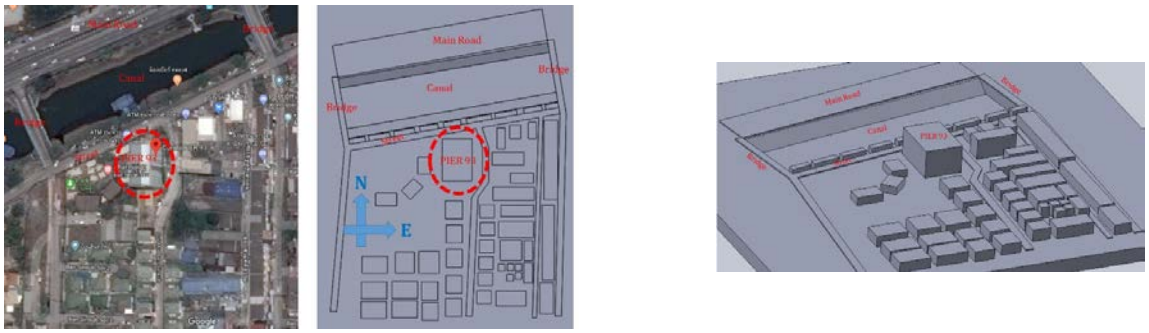

(a) (b) (c)

Fig. 15. Layout of terrain at PIER 93 (a) Google view (b) 2D Model view (c) 3D Model view.

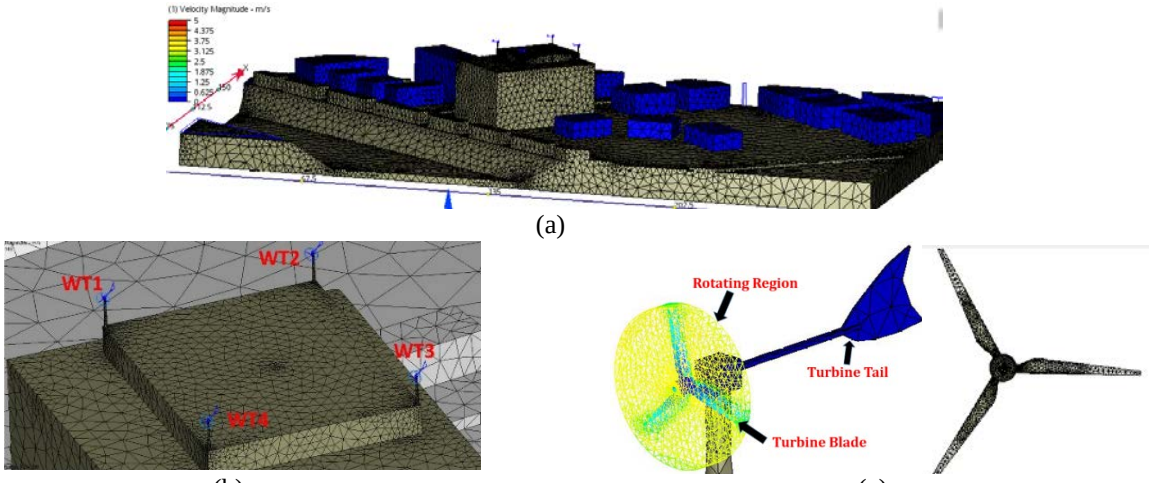

(a) (b) (c)

Fig. 16. 3D model grid cell for creating the (a) terrain, (b) roof top of PIER 93 building, (c) micro wind turbine.

Figure 17 shows the boundary condition imposed in the CFD model simulation, including the inlet side taking velocity of 3.82 m/s from the SSW and East–Northeast directions, and the outlet side taking pressure zero of the gage bar. On this model, the simulation included two primary conditions: the Static Part and Dynamic Part. The static part implies that the part does not move during the simulation. It includes the terrain, building turbine tail, and turbine nacelle. The dynamic part implies that the part moves during the simulation process. It includes the rotating region, turbine blade, and air particle

The simulation model type of the micro wind turbine in this research is simulated by the *free spinning* model condition. The torque is not considered in the free spinning model condition.

The grid dependence of the CFD simulation must be verified; in this case, the rotation of wind turbine number 1 (WT1) is the primary value for grid-dependence verification. Figure 18 shows the rotating of WT1 when using 3.82 m/s as the velocity of the inlet side, the rotating convert to 90 rpm at 5,000,000 grids cell which including wind turbine blade 2,500,000 cells, PIER 93 building 1,000,000 cells and terrain 1,500,000 cells.

2.2 PV and Battery Bank Calculation

The nominal peak (kWp) power of a solar array of n modules, each with a maximum power of Wp under the STC is expressed by

$$P_{peak} = \frac{E_{load} I_{STC}}{E_{glob} Q} \quad (1)$$

(a) (b)

Fig. 17. Boundary condition (a) velocity inlet from SSW direction (b) pressure outlet at outlet side.

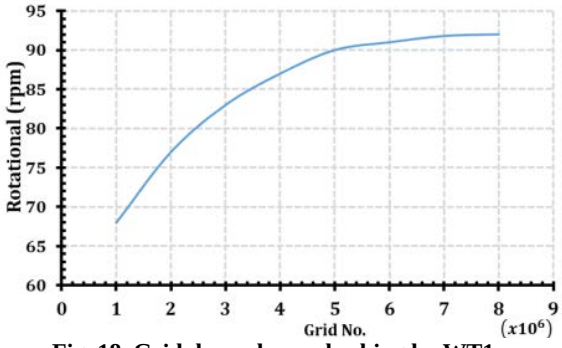

Fig. 18. Grid dependence checking by WT1.

where P_{peak} is the sum of the peak power under STCs of the photovoltaic solar panels (kWp); E_{load} is the electric energy produced by the PV panels (kWh/day); ISTC is the radiation under the STC (1 kW/m^2); E_{glob} is the global incident radiation (kWh/m^2·day); Q is the system quality.

The capacity of a battery depends on many factors such as solar energy, load, system reliability, and peak power of the system. In practice, the capacity of a battery is generally linearly related to peak power of the system with a slope of approximately 10, as shown in Figure 19.

The battery capacity (BC) can be described by the following equation:

$$C_B = 10P_{peak} \quad (2)$$

2.3 Micro Wind Turbine Calculation

Wind power is a function of wind speed, air density, swept area of blades, and the coefficient of performance (C_p):

$$P_w = C_p \frac{1}{2} \rho A v^3 \quad (3)$$

where P_w is the power of the urban wind turbine; C_p is the coefficient of performance; ρ is the air density; v is the wind speed; A is the swept area of the wind turbine. The maximum theoretical value of C_p is known as the Betz limit, which is 59%. However, for a typical commercial wind turbine, it is approximately 30%, and approximately 6% for a micro wind turbine [20], [21], [22]. As the rooftop area is limited, the system was designed as shown in Table 3.

In this study, a renewable hybrid system comprising PV and micro wind turbines was modelled. The daily wind speed profile for each month is shown in Figure 20. The modelling program (HOMER) that was used for the simulation contained values entered for various conditions: a load demand of approximately 21 kWh/day; PV of 4 kW; four sets of micro wind turbines, at 400 W each; 16 sets of 12 V, 200 Ah batteries.

The PV–wind hybrid simulation model, addition to the micro wind turbines and PV array, the system also includes the battery storage used to increase the system reliability. Primarily, the renewable sources feed the energy demand and excess energy is stored in the batteries.

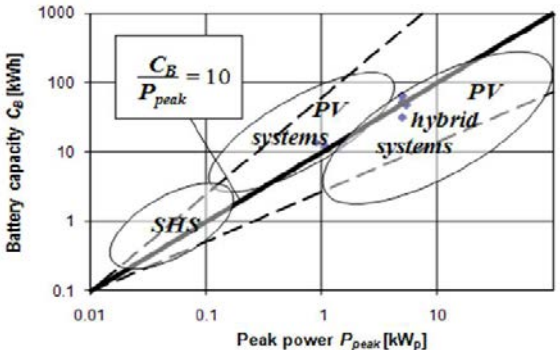

Fig. 19. Relationship between battery capacity and peak power [18].

Table 3. Type and capacity of combination renewable energy in the study system.

Type	Capacity
PV	4 kW
Micro wind turbine	650 W x 4

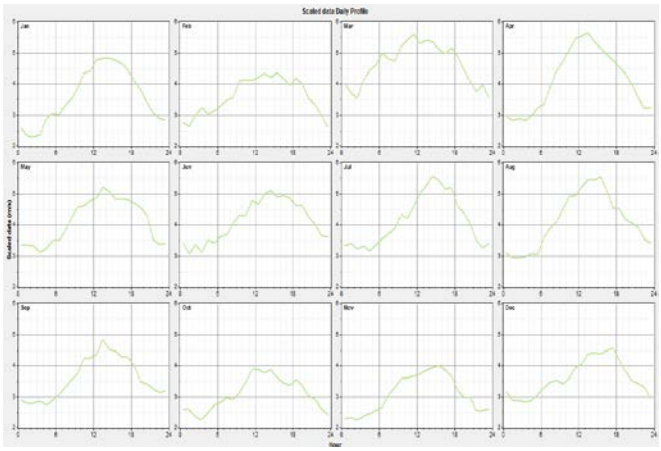

Fig. 20. Wind speed daily profile of HOMER program at 14 ˚N, 100 ˚E.

When renewable sources are not available, the batteries supply electricity to the system. In the system, a converter is used to convert DC power to AC power. Consequently, grid electricity can be used as an energy source to supplement renewable sources when required. However, as a stand-alone operation strategy has been adopted, this model does not transmit any power to the grid.

Figure 21 shows the simulation model of the hybrid PV and wind system. The overall PIER 93 building load demand is 29.15 kWh/d and the model includes a 4-kW PV system and 650-W micro wind turbine with batteries. The simulation system operated on the grid system type, solar resources using global solar radiation at the study site (14 ˚N, 100 ˚E), and wind resources shown in Table 1.

The micro wind turbine power curve is shown in Figure 22(a), illustrating that at 15 m/s incoming wind speed, the rated power of the turbine is 650 W. Figure 22(b) shows the monthly averages of the daily solar radiation and the clearness index for the study site over one year. The typical solar radiation at the site is found to be 5–6 kWh/m^2·day. At the site (14 ˚N, 100 ˚E), HOMER computes the scaled annual average of daily solar radiation as 5.37 kWh/m^2·day with an average sky clearness of 0.553.

As expected, solar radiation is available throughout the year, with the highest monthly average radiation in the Pathumthani Province (approximately 6.11 kW/m2·day) occurring in April, which is during the summer season. The lowest monthly average radiation values (approximately 4.96 kW/m^2·day) were recorded in November, which is the rainy season in Thailand.

2.4 Converter

Any system that contains both AC and DC elements requires a converter. A converter can be an inverter (to convert DC to AC), a rectifier (to convert AC to DC), or both. The size of the converter required to satisfy the peak demand in the study system was 3 kW, with a lifetime of 15 years. The inverter efficiency was 90%, and the rectifier efficiency was 85%.

2.5 Grid Input

The renewable-based hybrid system in this study utilized grid connectivity, which was conceptualized as a back-up energy source to compensate for the intermittency of solar and wind resources at the site. However, the model is stand-alone; implying any excess energy generated by it is not sold back into the grid.

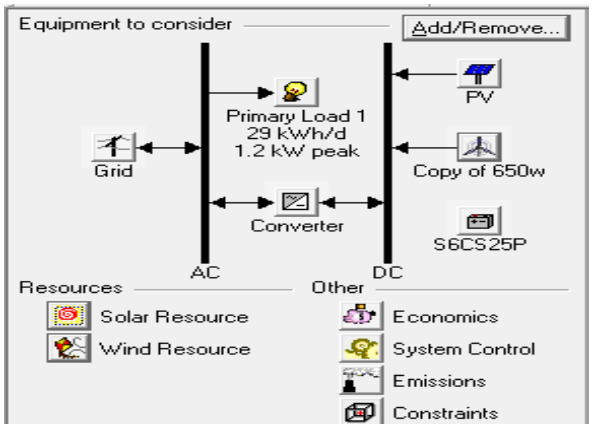

Fig. 21. Simulation model of the hybrid PV and wind system.

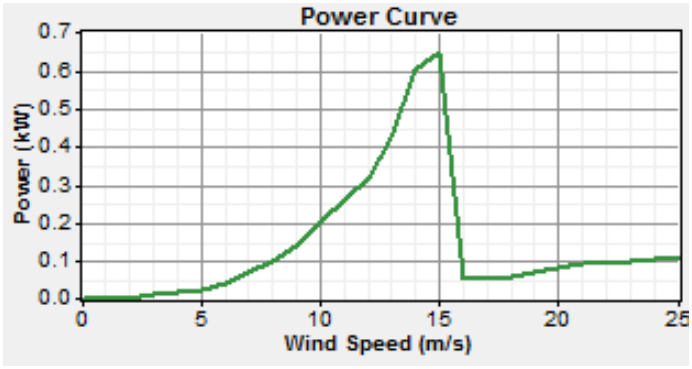

(a)

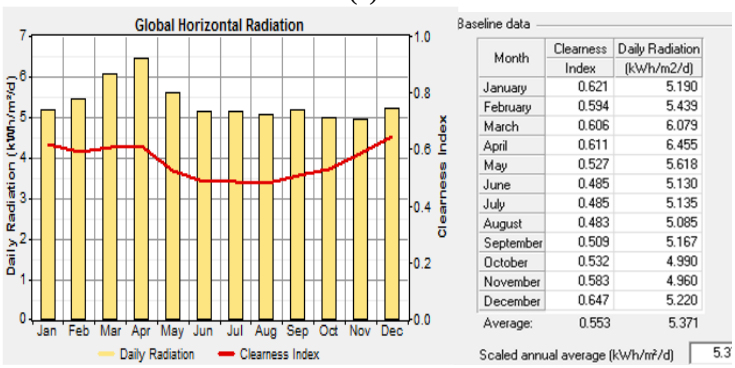

(b)

Fig. 22. Energy inputs for the wind turbine and solar photovoltaic array (a) power curve of micro wind turbine (b) global solar radiation at the study site (14 ˚N, 100 ˚E).

Table 4. Technical specifications of the PV panel used in this study.

	Specifications
Rated maximum power at STC	250 W
Maximum power voltage	30.5 V
Maximum power current	8.22 A
Module efficiency	15.4 %
Cell type	Polycrystalline n156 x 156 mm (6 inch)
Application class	A

Table 5. Technical specifications of the micro wind turbine used in this study.

	Specifications
Weight	15 kg
Rotor diameter	1.8 m
Rated power	650 W @ 15 m/s
Cut-in speed	3.0 m/s
Number of blades	3
Generator	PMG

2.6 Experimental Site Testing

The PV array is a collection of PV modules that generates DC electricity by collecting solar radiation. The lifetime of the PV arrays was assumed to be 25 years, and no tracking system was included in the PV system. The specifications of the PV rooftop panel used in the on-site experimental testing are shown in Table 4, and the specifications of the micro wind turbine are shown in Table 5.

The PV–wind hybrid power generating system installed on the rooftop of the PIER 93 building was comprised of a micro wind turbine of 650 W × 4 sets, PV array of 4 kW, backup storage batteries, and an inverter, and was integrated with the grid. Occasionally, power from the grid was provided to the hybrid system, either to equalize the charge of the batteries or to fulfil the site power demand during prolonged unfavourable weather conditions.

The hybrid system was equipped with data logging capacity to monitor various parameters, namely the solar current, wind current, load current, load power, PV power, and wind power, at one-minute intervals.

Figure 23 shows the on-site hybrid system on the rooftop. Figure 23a shows four sets of the 650-W micro wind turbine, and four sets of the PV panels that were installed on the rooftop building.

Figure 23b shows the PV panel, and Figure 23c shows the hybrid control panel that controls the PV and micro wind turbine systems.

The selected nominal voltage of the battery banks

in this study was 12 V, 200 Ah. The round trip efficiency for this type of battery is 80%, and the minimum state of charge is 40%.

The lifetime through the input value, i.e. the total amount of energy that can be cycled through the battery before a replacement is required, is 917 kWh. Figure 24a shows the correlation between the capacity (Ah) and discharge current (A). It indicates that the higher the discharge current, the lower is the capacity. Figure 24b shows 16 sets of the battery bank.

(a) (b) (c)

Fig. 23. Experimental hybrid system installed on the rooftop of PIER 93 building (a)Hybrid system on rooftop, comprising wind turbine and solar PV panels (b) PV panels installed on rooftop(c) Hybrid system.

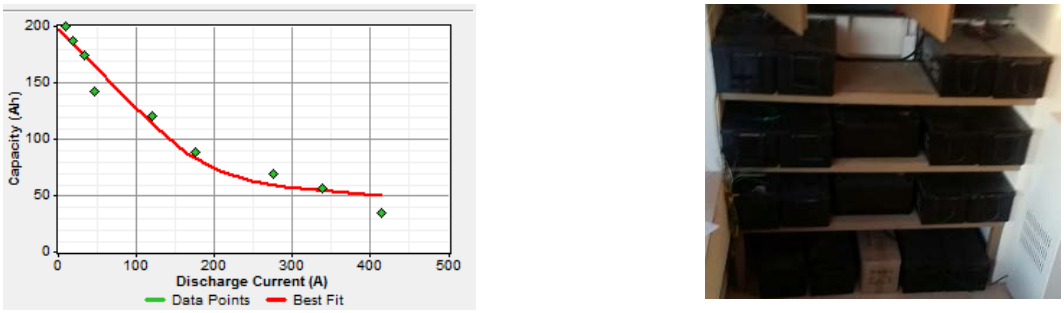

(a) (b)

Fig. 21. Specifications of battery banks used in this study (a) Battery capacity curve (b) Battery sets control panel.

3. RESULTS AND DISCUSSION

3.1 Computational Fluid Dynamics (CFD) Results

Figure 25 shows the overall points of velocity investigation that include points A to K. The magnitude velocity versus the height is as shown in Figure 26a. The height is between 0 and 26 m from the rooftop level. Owing to the tower of the micro wind turbine being 3 m, only the height between 0 and 3 m on the rooftop is considered for velocity profiles, as shown in Figure 26b.

The magnitude velocities at investigation points A–K is shown in Table 6. The velocity at 3 m high from the rooftop level of the CFD simulation result shows G > I > E > B > J > K > H > F > D > C. Owing to the total wind turbine being four sets, therefore four points were selected as the optimal location installation points: points A, E, G, and I.

Because only the wind turbine installing point is considered, WT1, WT2, WT3, and WT4 are installed at points A, C, F, and H, respectively. The magnitude velocity at 3 m high from rooftop level, the highest velocity is point G while the lowest velocity is point C. When the velocity magnitude that is the micro wind turbine installation point is considered, the result of the wind velocity is shown as WT1 > WT3 > WT4 > WT2.

Figure 27 shows the cross section velocity area of the East–Southeast (ESE) direction and SSW direction at each WT installation point, where the inlet wind flows from the SSW direction and the velocity magnitude is 3.82 m/s. Figure 28 shows the velocity contour of the SSW section at WT1, WT2, WT3, and WT4.

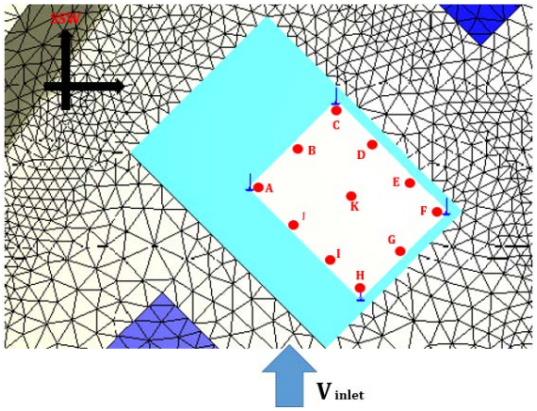

Fig. 25. Cross-section area of ESE direction and SSW direction at WT installation point.

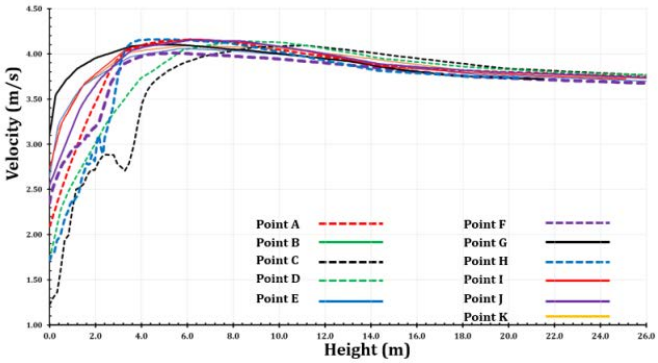

(a)

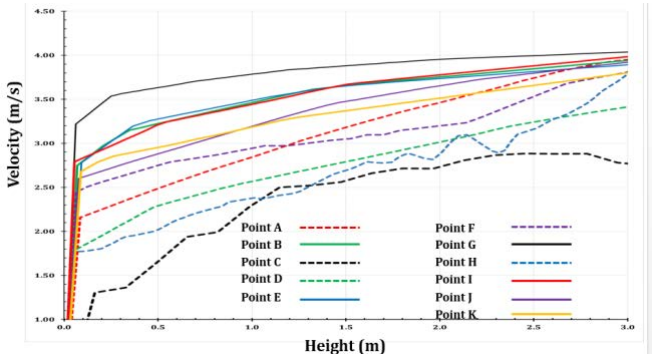

(b)

Fig. 26. Velocity distribution on rooftop from SSW wind flow direction (a) Height of 0–26 m from rooftop; (b) Height of 0–3m from rooftop.

Table 6. Velocity magnitude from SSW wind flow direction at point (A-K) of 3 m from rooftop level.

Point	V (m/s)	Point	V (m/s)
A (WT1)	4.05	B	4.02
C (WT2)	2.92	D	3.61
E	4.10	F (WT3)	3.82
G	4.33	H (WT4)	3.91
I	4.13	J	4.01
K	3.94		

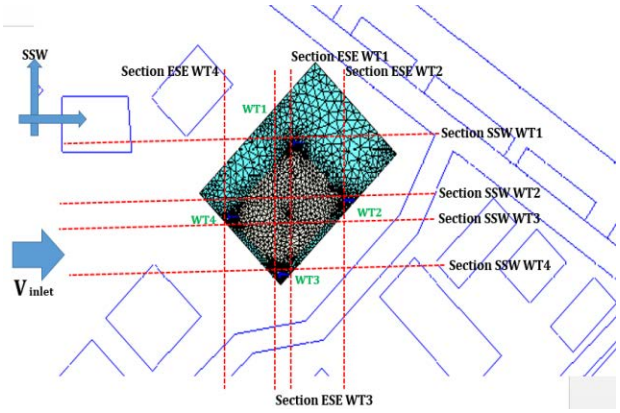

Fig. 27. Cross section area of ESE direction and SSW direction at WT installation point.

The wake flow region is generated at the downstream of the building area. Figure 29 shows the velocity contour and vector contour direction of the ESE section at WT1, WT2, WT3, and WT4 are shown as well.

These simulation results indicate that the magnitude velocity generated on the rooftop is higher than that generated on the building ground.

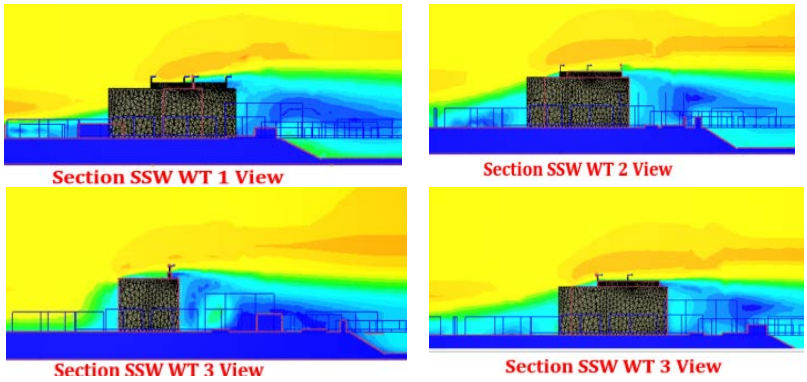

Fig. 28. Velocity contour of cross-section area SSW direction from SSW wind flow direction.

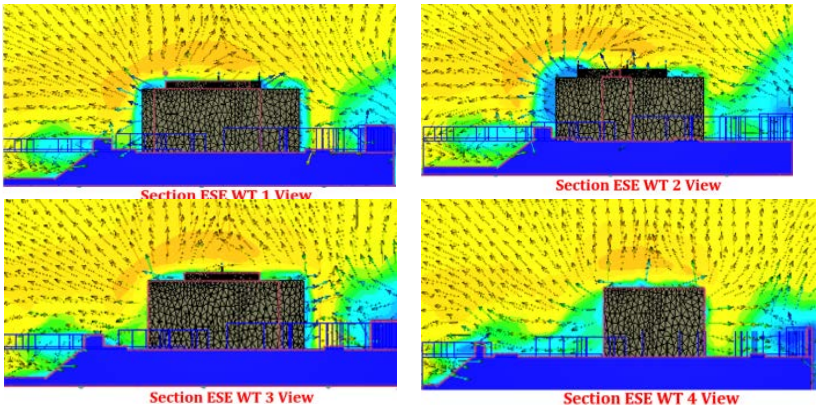

Fig. 29. Velocity and vector contour of cross section wind flow area of ESE section from SSW wind flow direction.

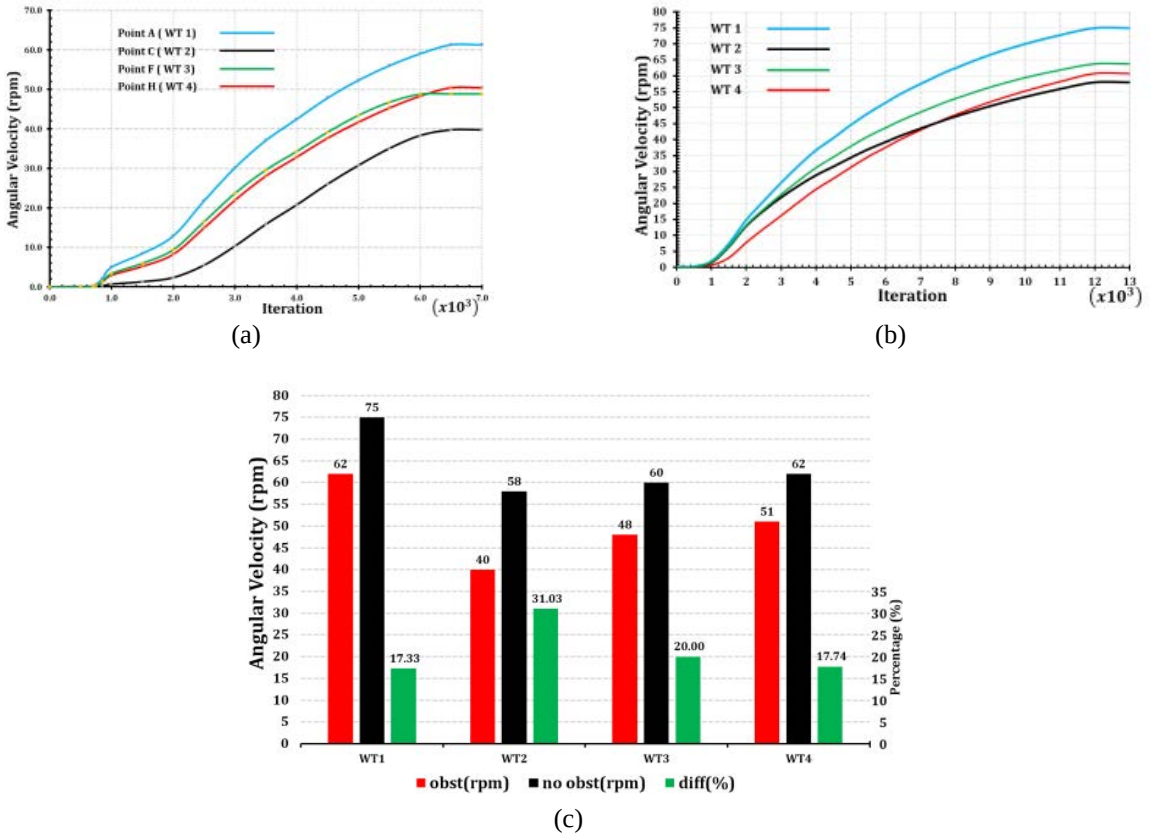

Fig. 30. Wind turbine velocity curve from SSW wind flow direction of WT1, WT2, WT3, and WT4 (a) including terrain obstacle, (b) not including terrain obstacle, (c) Percentage of angular velocity differences.

Figure 30 shows the result of the wind turbine velocity of WT1, WT2, WT3, and WT4; Figure 30a shows the result of the micro wind turbine when including the terrain obstacle; Figure 30b shows the result of the micro wind turbine when not including terrain obstacle; Figure 30c shows the percentage of velocity differences from the micro wind turbine.

Although the rooftop of the PIER 93 building that includes the terrain can generate a velocity higher than that of a no terrain landscape area (inlet velocity of 3.82 m/s), the rotation of the micro wind turbine lower is lower than that of the no obstacle case, as shown in Table 7.

3.2 New Location Installation Point

Considering the original micro wind turbine installation point as shown in Figure 31a, WT1, WT2, WT3, and WT4 are installed at the corners of the rooftop (points A, C, F, and H). The simulation results indicate that the optimal points that exhibit high velocities are points A, E, G, and I. These will be used for installing micro wind turbines WT1,WT2,WT3, and WT4, as shown in Figure 31b.

The results of the rotational of micro wind turbine at the new location installation are shown in Table 8 and Figure 32. As shown, the rotation of the turbine at the new location installation point including WT1, WT2, and WT3 are higher than that at the original location installation point, and lower than that of the no-obstacle simulation result. Meanwhile, the rotational value of the simulation of WT4 is higher than that of the original location point, and also higher than that of the no-obstacle case.

$$WT1_{ori} < WT1_{new} < WT1_{no\ obst}$$
$$WT2_{ori} < WT2_{new} < WT2_{no\ obst}$$
$$WT3_{ori} < WT3_{new} < WT3_{no\ obst}$$
$$WT4_{new} > WT4_{no\ obst} > WT4_{ori}$$

At WT4, the building created both the velocity magnitude and vector direction; therefore, the angular velocity (rpm) is increased (WT4new > WT4no obst > WT4ori) by approximately +27.45%, while WT1, WT2, WT3 are decreased by approximately −14.52, −27.51, and −14.58, respectively.

3.3 HOMER Result

The wind turbine used in this study was four sets of 650 W, yielding 2.6 kW; meanwhile, the PV panel system was 4 kW, as shown in Figure 33a for the wind turbine and Figure 33b for PV.

An average daily profile of the power output of the wind turbine and PV for each month is shown in Figure 34. As shown in Figure 34a, the highest wind energy was generated in March (approximately 0.35 kW), while the lowest was generated in October (approximately 0.1 kW). Throughout the year, the PV power output remained relatively constant, as shown in Figure 34b.

Table 7. Rotating of micro wind turbine between including terrain obstacle and not including terrain obstacle from the SSW wind flow direction.

Point	Obst (rpm)	No obst (rpm)	Diff (%)
WT1	62	75	-17.33
WT2	40	58	-31.03
WT3	48	60	-20.01
WT4	51	62	-17.74

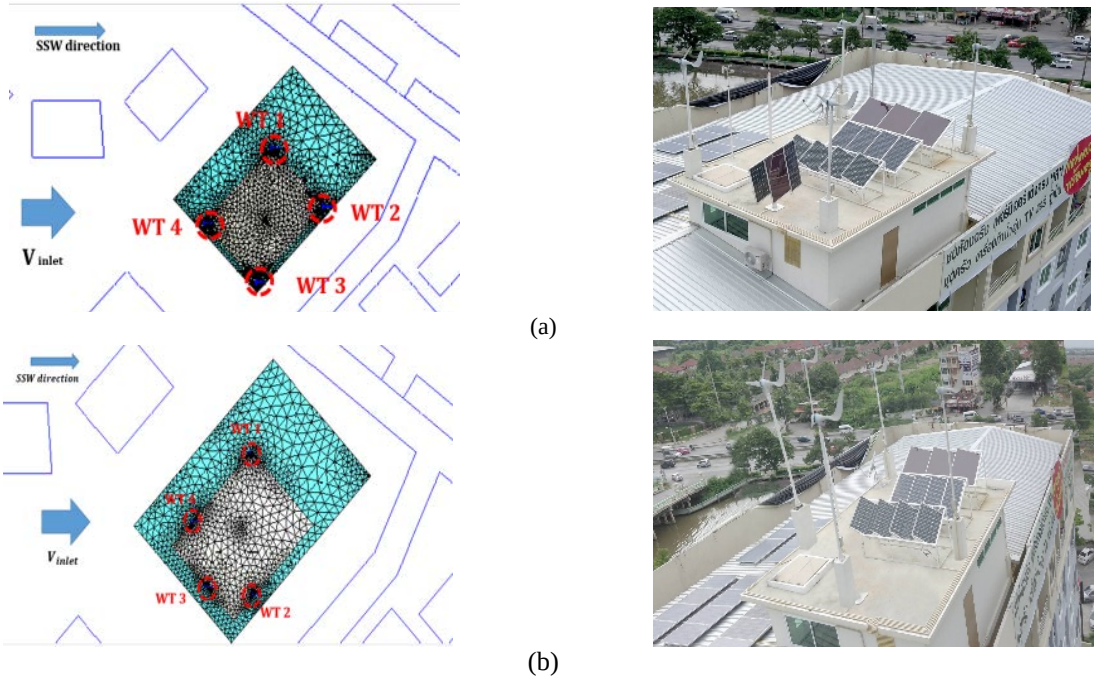

Fig. 31. Micro wind turbine installation point (a) original location point (b) new location point.

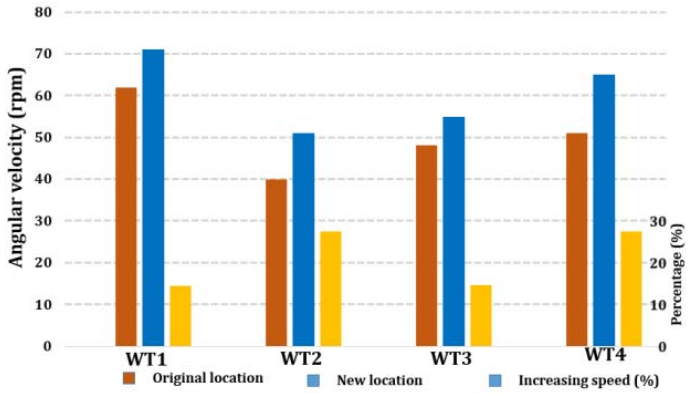

Fig. 32. Percentage of angular velocity differences from SSW wind flow direction.

Table 8. Rotation of micro wind turbine between original location and new location from SSW wind flow direction.

Point	Original (rpm)	New (rpm)	Diff (%)
WT1	62	71	-14.52
WT2	40	51	-27.51
WT3	48	55	-14.58
WT4	51	65	+27.45

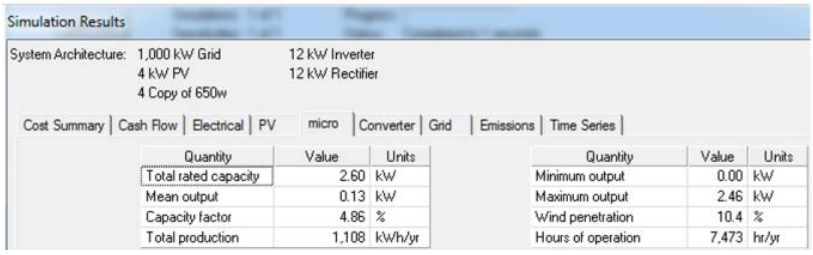

(a)

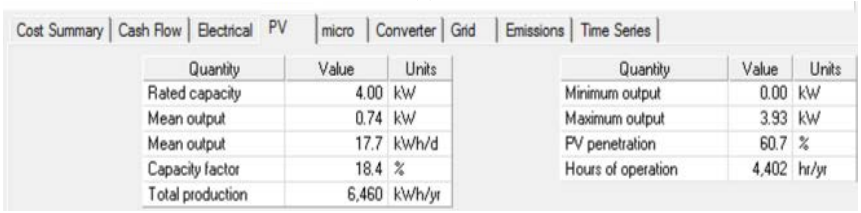

(b)

Fig. 33. Electricity production of HOMER simulation result of hybrid wind–PV system, (a) wind turbine simulation result, (b) PV simulation result.

3.4 Electricity Production

The monthly average electricity production of the entire PV–wind hybrid system, as calculated with HOMER, is shown in Figure 35.

The results in Table 9 and Table 10 indicate that the annual electrical energy from the hybrid system that is available to fulfill the demand is 10,640 kWh. Further, 47% (6,460 kWh/y) of this electricity is produced by the solar panels, while 8% (1,108 kWh/y) and 45% (6,187 kWh/y) are supplied by the wind turbine units and the grid, respectively. The mean PV and wind turbine outputs were found to be 740 W and 130 W, respectively. The overall renewable contribution to the total electricity share was found to be 52.4%.

Table 11 shows the HOMER simulation results of the monthy energy purchased. The maximum value is 386 W in October, which is the rainy season with little sun irradiation.

The minimum value is 232 W, in April, which is the summer season with high sun irradiation.

Figure 36 compares the HOMER simulation results with the on-site experimental values recorded for the wind turbine. The data were recorded from February 2016 to January 2017.

In general, the average micro wind turbine power production was found to be relatively higher from October to February in comparison to the remainder of the year.

The estimated wind turbine power-production from the HOMER simulation was consistently higher than the measured on-site values throughout the year, with an average difference of 26.65%. This can be attributed to the fact that the real site has many parameter effects such as wind gusts, building obstructions, and the Venturi effects, although the micro wind turbine responds to changes in the wind direction.

The simulated and experimental values for energy production from each of the renewable energy sources in the system studied is shown in Table 12.

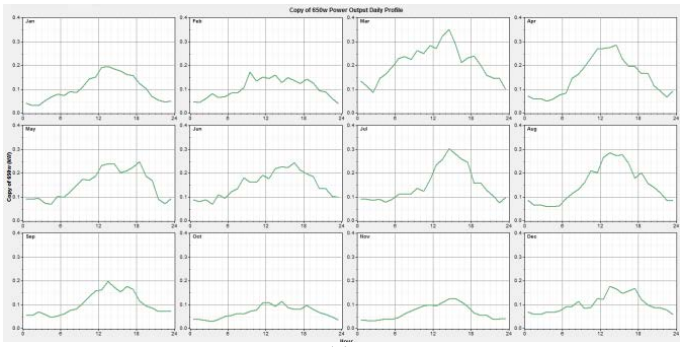

(a)

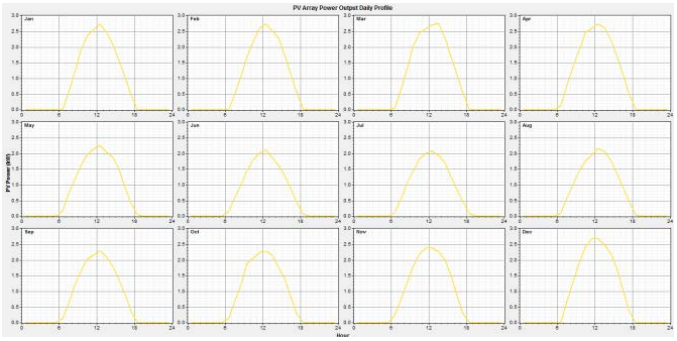

(b)

Fig. 34. Average daily power output profiles by month for case study hybrid power; (a)Wind turbine power output (b) PV power output.

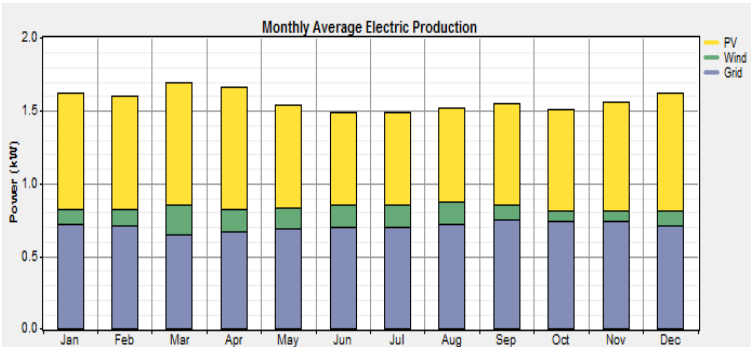

Fig. 35. Monthly averages of energy output from case study hybrid renewable energy system, as calculated with HOMER.

Table 9. Simulation results of a hybrid PV–wind energy system operating on PIER 93 building.

Parameter	Value
PV array rated capacity	4 kW
Mean output	0.74 kW, 17.77 kWh/day
Capacity factor	18.4%
Total production	6,460 hr/day
PV penetration	60.7%
Hours of operation	4,402 hr/day

Table 10. Simulation results of a hybrid PV–wind energy system operating on PIER 93 building.

Parameter	Value
Wind turbine rated capacity	2.6 kW
Mean output	0.13 kW, 3.04 kWh/day
Capacity factor	4.86%
Total production	1,108 hr/day
PV penetration	10.4%
Hours of operation	7,473 hr/day

Table 11. HOMER simulation result of monthly energy purchased.

Month	Energy purchased (kWh)	Month	Energy purchased (kWh)	Month	Energy purchased (kWh)
Jan	303	May	330	Sep	357
Feb	276	Jun	364	Oct	386
Mar	203	Jul	375	Nov	345
Apr	232	Aug	366	Dec	291
				Annual Average	3,829 kWh

Table 12. Power production (simulated with HOMER and experimentally) of the renewable energy sources in a hybrid wind–PV energy system installed on Pier 93 building.

Type	Simulated (kWh/y)	Experimental (kWh/y)	Difference (%)
PV	6,460	5,825	9.87
Wind turbine	1,108	812	26.65

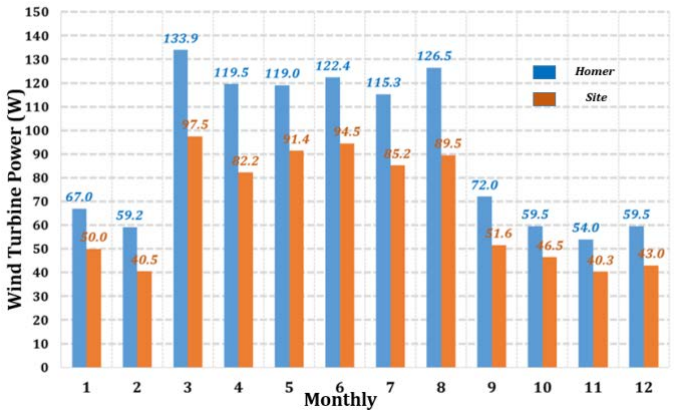

Fig. 36. Comparison between HOMER simulation and on-site experimental values for monthly micro wind turbine power production (Feb. 2016 to Jan. 2017).

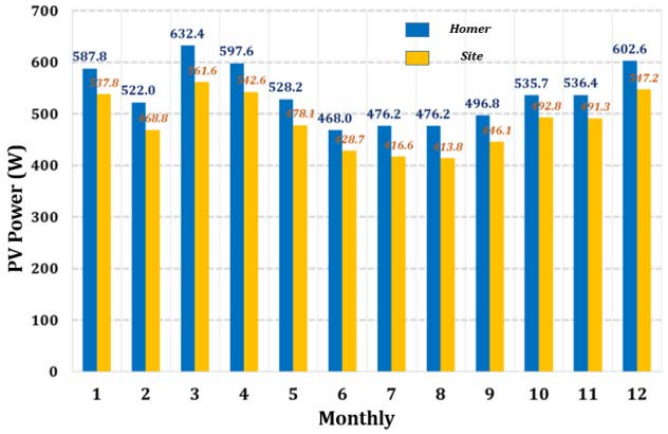

Fig. 37. Comparison between HOMER simulation and on-site experimental values for monthly solar photovoltaic power production (Feb. 2016 to Jan. 2017).

Figure 37 shows a comparison between the values estimated by the HOMER simulation and the on-site experimental values of the power produced by PV. The data were recorded from February 2016 to January 2017. The HOMER-estimated PV power production was higher than the actual on-site values recorded throughout the year, with an average difference of 9.87%. The monthly average electricity production of the entire PV–wind hybrid system is shown in Figure 38, as measured on-site during one year.

The figure shows that the PV power generation is promising almost all year round. The annual average power production from the combination of renewable energy sources was 18.19 kWh/d, of which the PV and wind turbine outputs were found to contribute 662.86 W and 92.35 W on average, respectively.

The annual average renewable contribution to the total electricity share was found to be 52.4%, thus reinforcing the idea that solar and wind power production possess good monthly complementarity.

Figure 39 shows the monthly power purchased from the grid to supplement the renewable energy in the hybrid system. The lowest level of support from the grid was in April, thereby resulting in the high solar radiation and high wind in that month at the study site.

Figure 40 shows the monthly power production of the hybrid wind–PV energy system from the HOMER simulation result. The highest grid purchase was in March (approximately 632.4 kWh) and the lowest was in June (approximately 468.0 kWh).

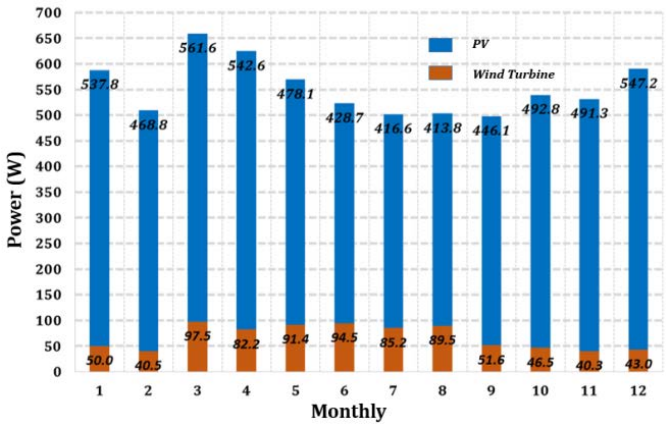

Fig. 38. Site measurement data of monthly average electricity production, measured on-site, of a hybrid PV-wind energy system installed at PIER 93 Building.

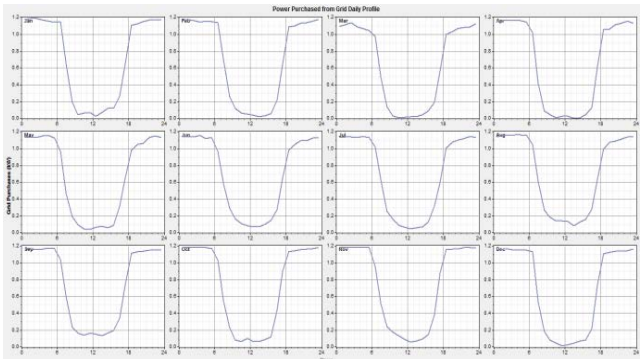

Fig. 39. HOMER result of monthly profiles of power purchased from grid into a hybrid wind-PV energy system installed on PIER 93 building.

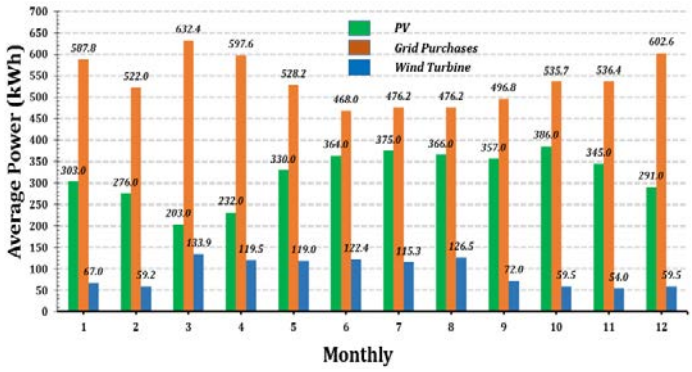

Fig. 40. Monthly power production of hybrid wind-PV energy system from HOMER simulation result.

4. CONCLUSION

This paper presented a feasibility study of a PV–wind hybrid power system, along with the experimental data gathered from such system, established on a high-rise building located in the Pathum Thani Province.

The CFD simulation result demonstrated the rotational speed of the micro wind turbine, although the terrain and PIER 93 building could increase the wind velocity magnitude, but the rotation of the micro wind turbine decreased because the rotation was of the vector type, which depended on the magnitude and direction. The CFD rotating condition type is important and should be incorporated for wind turbine simulations.

Generally, the rotation of wind turbine is WTori < WTnew < WTno obst. However, the result of WT4 is WT4new > WT4no obst > WT4ori, indicating that some points on the rooftop can increase both the velocity magnitude and vector velocity direction.

The experimental system was grid connected and designed using the HOMER software, considering selected location data such as global solar radiation, wind speed, and daily load demand.

The HOMER simulation results of the system output indicated that 47% of the electricity was produced from solar PV panels, while 8% was from wind energy; therefore, 45% of the electricity demanded from the grid can be replaced with renewable energy. The experimental results recorded on site indicated that 42.38% of the energy supplied to the hybrid system was from the PV panels, while an average of 5.87% of the energy was produced by the wind turbine system annually. This indicated that the hybrid PV–wind energy

system could reduce the annual dependence on the grid electricity by 51.75%.

The CFD method was a good option for considering the optimal locations for wind turbine installation although the complex flow of urban terrains were involved, whereas the HOMER software was beneficial for investigating the hybrid renewable energy system while considering the annual electricity production.

ACKNOWLEDGEMENT

The authors would like to thank all that assisted in this study including the team in Energy Research and Service Center (ERSC) of engineering faculty, RMUTT who supported the work and helped in getting quality and accurate analysis. The authors are very grateful to, Asst. Prof. Dr. Wirachai Roynarin for his patience and support in overcoming numerous obstacles in the process of conducting this study. Additionally, the authors would like to thank all friends who supported and gave motivation in one way or another. The authors would also like to thank their families for their spiritually encouragement throughout the writing process of this paper.

REFERENCES

[1] Subhadeep B. and A. Shantanu. 2015. PV–wind hybrid power option for a low wind topography. *Energy Conversion and Management* 89: 942-954.

[2] Chua K.H., Lim Y.S., and Morris S., 2015. Cost-benefit assessment of energy storage for utility and customers: a case study in Malaysia. *Energy Convers Management* 106:1071–1081.

[3] Vikas K., Savita N., and Prashant B., 2016. Solar–wind hybrid renewable energy system: A review. *Renewable and Sustainable Energy Reviews* 58: 23-33.

[4] Sunanda S. and S.S. Chandel. 2015. Prospects of solar photovoltaic–micro-wind based hybrid power systems in western Himalayan state of Himachal Pradesh in India. *Energy Conversion and Management* 105:1340-1351.

[5] Saidur R., Rahim N.A., Islam M.R., and Solangi K.H., 2011. Environmental impact of wind energy. *Renewable and Sustainable Energy Reviews* 15:2423–2430.

[6] Moller H. and C.S. Pedersen. 2011. Low-frequency noise from large wind turbines. J *Acoust Soc Am* 129: 3727–3744.

[7] Regulation PEA on the terms of network connectivity. 2008.

[8] Solar Energy Division. 2010. Department of Alternative Energy Development and Efficiency. Ministry of Energy, Thailand. *Guide for development and investment on energy production*. 2010. Vol.2.

[9] Kang G., Kim J., Kim D., Choi W., and Park S., 2017. Development of a computational fluid dynamics model with tree drag parameterizations: Application to pedestrian wind comfort in an urban area. *Building and Environment* 124: 209-218.

[10] https://www.windfinder.com/forecast/suvarnaphumi_airport

[11] Manwell, J.F., Mcgowan, J.G., and Rogers, A.L., 2009. Wind Energy Explained: Theory, Design and Application.

[12] Zhao Y.S., Zhan J., Zhang Y., Wang D.P., and Zou B.G., 2009. The optimal capacity con figuration of an independent wind/PV hybrid power supply system based on improved PSO algorithm. In *Proceedings of APSCOM-IEEE*, pp. 1-7.

[13] Gupta R.A., Kumar R., and Bansal A.K., 2012. Economic analysis and design of standalone wind/PV hybrid energy systems using genetic algorithm. In *Proceedings of ICCCA*, pp. 1-6.

[14] Sharp J.K., 1981. Consumer incentives for solar energy. In *Proceedings of IEEE*, pp. 849–851.

[15] Kekezoglu B., Arikan O., Erduman A., Isen E., Durusu A., and Bozkurt A., 2013. Reliability Analysis of hybrid energy system: case study of Davutpasa campus. *Proceedings of EUROCON*, pp. 1141-1144.

[16] Ma T., Yang H., and Lu L., 2014. A feasibility study of a standalone hybrid solar–wind battery system for a remote island. *Applied Energy* 121: 149–158.

[17] Chong W.T., Naghavi M.S., and Poh S.C., 2011. Techno-economic analysis of a wind–solar hybrid renewable energy system with rain water collection feature for urban high rise application. *Applied Energy* 88: 4067–4077.

[18] Sinha S and S.S. Chandel. 2013. Prefeasibility analysis of solar wind hybrid system potential in a complex hilly terrain. *Int J Eng Technol Adv Eng* 3: 277–282.

[19] Cooney C., Byrne R., Lyons W., and O'Rourke F., 2017. Performance characterisation of a commercial-scale wind turbine operating in an urban environment, using real data. *Energy for Sustainable Development* 36: 46–54

[20] Zakaria M.Y., Pereira D.A., and Hajj M.R., 2015. Experimental investigation and performance modeling of centimeter-scale micro-wind turbine energy harvesters. *J. Wind Eng. Ind. Aerodynamics* 147:5 8-65.

[21] Leung D., Deng Y., and Leung M., 2010. Design optimization of a cost-effective micro wind turbine. *In World Congress on Engineering*, London.

[22] Xu F., Yuan F., Liu L., Hu J., and Qiu Y., 2013. Performance prediction and demonstration of a miniature horizontal Axis wind turbine. *J. Energy Eng.* 139: 143-152.